Doped MoS₂ Polymorph for an Improved Hydrogen Evolution Reaction

Håkon Eidsvåg,* Ponniah Vajeeston, and Dhayalan Velauthapillai

Read Online

ACCESS | Metrics & More | Article Recommendations | SI Supporting Information

ABSTRACT: Green hydrogen produced from solar energy could be one of the solutions to the growing energy shortage as non-renewable energy sources are phased out. However, the current catalyst materials used for photocatalytic water splitting (PWS) cannot compete with other renewable technologies when it comes to efficiency and production cost. Transition-metal dichalcogenides, such as molybdenum disulfides (MoS_2), have previously proven to have electronic and optical properties that could tackle these challenges. In this work, optical properties, the d-band center, and Gibbs free energy are calculated for seven MoS_2 polymorphs using first-principles calculations and density functional theory (DFT) to show that they could be suitable as photocatalysts for PWS. Out of the seven, the two polymorphs $3H_a$ and $2R_1$ were shown to have d-band center values closest to the optimal value, while the Gibbs free energy for all seven polymorphs was within 5% of each other. In a previous study, we found that $3H_b$ had the highest electron mobility among all seven polymorphs and an optimal bandgap for photocatalytic reactions. The $3H_b$ polymorphs were therefore selected for further study. An in-depth analysis of the enhancement of the electronic properties and the Gibbs free energy through substitutional doping with Al, Co, N, and Ni was carried out. For the very first time, substitutional doping of MoS_2 was attempted. We found that replacing one Mo atom with Al, Co, I, N, and Ni lowered the Gibbs free energy by a factor of 10, which would increase the hydrogen evolution reaction of the catalyst. Our study further shows that $3H_b$ with one S atom replaced with Al, Co, I, N, or Ni is dynamically and mechanically stable, while for $3H_b$, replacing one Mo atom with Al and Ni makes the structure stable. Based on the low Gibbs free energy, stability, and electronic bandgap $3H_b$, MoS_2 doped with Al for one Mo atom emerges as a promising candidate for photocatalytic water splitting.
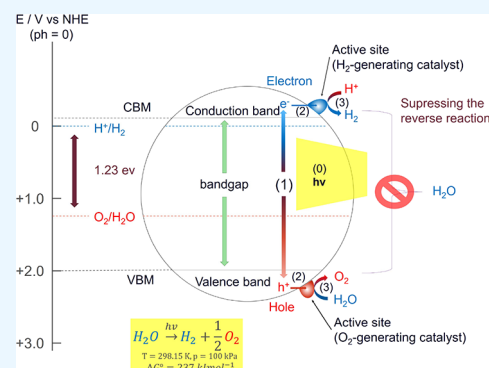
1. INTRODUCTION

Hydrogen produced from water and powered by solar energy is considered one of the most profitable and sustainable alternatives to fossil fuels due to the abundance of water and sunlight. Several technologies are being developed to obtain hydrogen from water, such as electrolysis, photolysis, biological treatment techniques, and thermolysis.[1] Of these, photocatalytic water splitting is seen as one of the most promising technologies due to its low production cost, good solar-to-hydrogen (STH) efficiency, ease of hydrogen and oxygen separation, and the possibility of both large- and small-scale facilities.[2−4] However, the current achieved STH, lifetime, and production costs are not good enough to warrant large-scale production facilities.[5,6]

Transition-metal dichalcogenides have been seen as a possible solution to tackle these challenges due to their intriguing electronic and optical properties.[7] Especially MoS_2, with its catalytic properties,[8,9] could be a promising photocatalytic candidate. Atomically MoS_2 is a thin material, which means that the catalytic active sites are exposed to the reactants. This feature increases the efficiency of the chemical process. MoS_2 is also already used in industry as a catalyst, with established and optimized production methods making it a low-cost material.[10] Recent work has looked into how MoS_2 can be used for

photocatalytic degradation of dyes and found that it is very effective toward organic dyes and organic and toxic pollutants.[11−13] This is because MoS_2 photocatalyzes in the visible region, it has a high specific surface area and an efficient charge separation, and it exists in several different polymorphs.[14] Through small modifications of the compound composition, crystal structure, or production method, the performance of MoS_2 can be significantly altered.[15−20] The inclusion of dopants or changes in crystal structure has a large impact on the catalytic activity by changing the electronic and optical structure of MoS_2. This makes it possible to alter the MoS_2 structure in such a way that the STH efficiency is increased. Over the past years, research into MoS_2 as a catalyst and cocatalyst for photocatalytic water splitting has increased.[18,21−24] In a previous article, we investigated 14 different MoS_2 polymorphs using density

functional theory calculations. Here, we found that seven of these polymorphs were both dynamically and mechanically stable and that they have bandgaps in the range of 1.87 to 2.12 eV.[25] This makes them interesting and viable candidates for photocatalytic water splitting.

In this article, we will therefore investigate these seven MoS_2 polymorphs further and look into properties influencing their photocatalytic water-splitting potential. The d-band center and Gibbs free energy are used as descriptors for the potential hydrogen production, and the obtained values are compared to the existing literature. In addition, we explore if there are any temperature-dependent phase transitions in the structures and we obtain their absorption spectra. This provides us with a clear overview of the different polymorph's potential as a catalyst for photocatalytic water splitting.

Based on these results and the results from our previous paper,[25] one of the polymorphs ($3H_b$-MoS_2) was selected for further experimentation as it was deemed to have the highest potential for PWS based on its absorption spectra, bandgap, and high electron mobility. It was decided to dope $3H_b$-MoS_2 with Al, Co, I, N, and Ni to see how that would affect the Gibbs free energy and the band structure. We chose these elements based on existing work and as they represent a wide array of metals and non-metals. Al-doped MoS_2 has been proven to be a stable configuration with tunable carrier density,[26] and it has shown promise as a catalyst for CO oxidation.[27] In combination with g-C_3N_4, Co-doped MoS_2 shows promise as an effective photocatalyst due to the distortions in the MoS_2 induced by Co atoms.[28] Co-doped MoS_2 has also been shown to give good results as an HER catalyst for electrochemical water splitting.[29] N and Ni as dopants have improved the catalytic performance of MoS_2 for electrochemical water splitting.[30] It is reported that the catalytic current density of N-doped MoS_2 can reach 15 times that of pristine MoS_2.[31] Ni on the other hand was found to add more electrochemical sites, improve the conductivity of the catalyst, and increase the turnover frequency.[32] Although other halogens such as Cl and F have been used with success to activate both the basal plane sites[30] and the edge sites,[33] no work has been done with I. Based on this did we decide to use I as a dopant here to investigate how it would affect MoS_2 and its photocatalytic properties. Through DFT calculations, the effects of substitutional doping (both Mo and S were replaced with the dopants) on Gibbs free energy, bandgap, optical spectra, stability, and charge density were investigated. Showcasing that through doping, it is possible to create MoS_2 catalysts that have the potential of a high STH efficiency.

2. COMPUTATIONAL METHOD

Every calculation was performed using the periodic density functional theory framework through the VASP code.[34−38] We used the projector-augmented wave (PAW) method to describe the interaction between the core (Mo:[Kr] and S:[Ne]) and the valence electrons.[37,39] The structures were optimized using the Perdew−Burke−Ernzerhof (PBE) exchange-correlation functional and further optimized with the DFT/vdW-DF2 method.[40−42] For the phonon calculations, the supercell method was used. The real space force constants of the supercell were calculated with the VASP code, and then the PHONOPY code was used to calculate the phonon frequencies from the force constants in the supercell consisting of at least 32 atoms in all systems. Every atom was displaced by a finite displacement of 0.01 Å in the x, y, and z directions to get the force-constant matrices for each binary system. $4 \times 4 \times 4$ **k** points and strict

energy convergence criteria (10^{-8} eV) were used for the force constant calculations. We then built a dynamical matrix for the different **q** vectors in the Brillouin zone. By solving this matrix, the phonon frequency eigenvalues and phonon mode eigenvector were found. The PHONOPY[43] code was then used to calculate the thermodynamic properties through a summation of the phonon eigenvectors. Based on this the energy versus temperature curves were generated. Our previous calculations suggested[44] that structural parameters in oxides could be reliably predicted only by using a large energy cutoff to guarantee basis-set completeness. Hence, we have used a cutoff of 500 eV. The electronic properties were computed by using the screened hybrid functional as proposed by Heyd, Scuseria, and Ernzerhof (HSE06) and generalized gradient approximation (GGA + U) for the polymorphs optimized at the PBE level.[45] If not specified differently, we used a Monkhorst−Pack $9 \times 9 \times 9$ **k** mesh for the structural optimization and the electronic polymorph studies. Band polymorphs were computed by solving the periodic Kohn−Sham equation on 10 **k** points along each direction of high symmetry of the irreducible part of the first Brillouin zone. Gibbs free energy and optical properties were calculated using a Gamma $8 \times 8 \times 1$ **k** mesh. VASPKIT[46] and SUMO[47] have been used for postprocessing and plot production. For the doped structures, GGA + U was used for the bandgap calculations; see Table 1 for the chosen U values.

Table 1. U Values Chosen for the GGA + U Calculations

atom	U
Mo	3.28[48]
S	4.0[48]
Al	4.0[49]
Co	3.0[50]
I	8.0[51]
N	7.0[52]
Ni	6.0[53]

3. RESULTS AND DISCUSSION

3.1. Energy vs Volume and Temperature Dependency. MoS_2 can exist in several different crystal polymorphs or polytypes in three dimensions due to the large variation in stacking sequences and the number of successive S−Mo−S sandwiches along the hexagonal c axis. The different variants are called 1T, 2H, 3R, $4H_a$, and 6R. Here, the integer stands for the number of S−Mo−S sandwiches per unit cell along the hexagonal c axis, while the T, H, and R indicate the type of symmetry: tetragonal, hexagonal, and rhombohedral, respectively. In our previous work, we studied 14 novel polymorphs to understand how the stacking sequence and layer−layer distance influence the properties of the compound.[25] Seven of these were found to be both mechanically and dynamically stable, making them interesting for further research.[25] To increase our understanding of the properties of the polymorph, we have now investigated how temperature would influence the relative stability of the polymorphs and if it would induce any phase transitions. Figure 1 shows energy versus temperature curves for the seven stable polymorphs. The starting point for these calculations was the preferred volume found in our previous work. As seen below, increasing the temperature does not change the relative stability between the polymorphs. In fact, only between 400 and 600 K, we can see a small deviation and $3H_a$ transitions to be the most stable polymorph at 500 K.
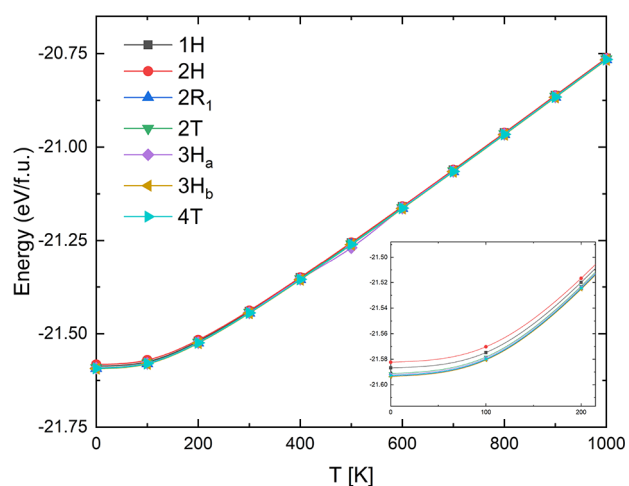
Figure 1. Energy vs temperature curve for the seven studied polymorphs. Zoomed-in insert between 0 and 200 K is added to show the small difference between the structures.

However, the change is only 0.9 eV as seen in Figure 1 and we believe that this phase transition is a numerical artifact caused by the calculation. This means that temperature is not a large factor for these polymorphs and one can choose the most appropriate one for a specific application without having to consider phase transitions.

3.2. Optical Properties. In 1996, Norskov and co-workers proposed the d-band center theory, which correlates the energy of the d-band center of gravity of a metal catalyst with the adsorption energy, activation energy, and dissociation energy of small molecules.[54,55] They state that the electron density of states (DOS) close to the Fermi level is correlated to the adsorbate substrate adsorption energy due to interactions between electrons occupying d-type orbitals of the metal (d-band) and those of the adsorbate.[54,55] In general, if the d-band center is downshifted compared to the Fermi level, it is an indication of good catalytic activity.

Although there have been significant efforts to verify the d-band theory, it has not been proven to be valid for all systems. In general, more complex systems have other factors, not included in the d-band center theory, influencing the catalytic activity. However, our systems are deemed to be of a simple enough character that the d-band center will indicate the catalytic activity. Pt is considered to have an optimal position for the d-band center for the most favorable hydrogen binding energy, -1.929 eV with respect to the Fermi level.[56] Our results are presented in Table 2 below. 1H and 2T have positively shifted d-band centers compared to the Fermi level; in addition, they are far away from the optimal value of -1.929 eV. This means that they have higher energy in the antibonding states and the bond between the structure surface and adsorbed material will be

higher,[57,58] leading to a decrease in the chance of photocatalytic reactions. However, the closer the d-band center is to the Fermi level, the better charge carrier transfer.[59] 2H, 2R$_1$, 3H$_a$, 3H$_b$, and 4T have downshifted d-band centers, indicating that they could be effective photocatalysts, especially 2R$_1$ and 3H$_a$, -1.520 and -1.541 eV, respectively, which have d-band center values not far from the optimal value of -1.929 eV. The binding strength of H will be less compared to that of the other structures, thus demanding less energy to be removed from the surface and create H$_2$ atoms.
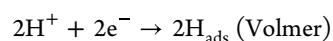
An important parameter for a catalyst used for photocatalytic water splitting is the absorption coefficient as it determines how far into the material the light will travel before it is absorbed. For water-splitting applications, the catalytic materials must have a high absorption coefficient in the visible region, to ensure that photons are absorbed. In addition to the absorption coefficient, we have also calculated the refractive index of the material to better understand the optical properties of the polymorphs.

All the polymorphs showcase the same rise in absorption coefficient, see Figure 2a, at 2 eV (620 nm), which corresponds to orange light, followed by a larger and wider upswing at 2.7 to 3.5 eV (460 to 355 nm), which is in the blue and violet range of visible light. This indicates that polymorphs can absorb photons at both ends of the visible light spectra, but there is still a considerable number of photons not absorbed. This could be remedied by introducing dopants that would influence the optical properties of the polymorphs, making the polymorphs tuned for the specific needs of photocatalytic water splitting.

Our calculations show that 2R$_1$ (2.67×10^5 cm^{-1}) has the highest absorption coefficient within the visible spectra. It is closely followed by 2H and 3H$_b$ at 2.33×10^5 and 2.28×10^5 cm^{-1}, while 1H has the lowest absorption coefficient (1.62×10^5 cm^{-1}) in the visible region. 2R$_1$, 2H, and 3H$_b$ are, based on the absorption coefficient, the best candidates for photocatalytic water splitting.

The refractive index (Figure 2b) of the material determines how light propagates inside a material, and the higher the refractive index, the slower light will travel through the material. This results in higher irradiance in the material, which enhances the photocatalytic activity of the material. We see that 2R$_1$, 2H, and 3H$_b$ have the largest peaks around 5 in the visible region. This means that they are classified as high refractive index materials ($n > 3.9$),[60] making them ideal candidates for photonic devices such as solar cells, photonic crystals, and PWS. This is because they have a larger scattering cross section[61] and smaller mode volumes[62] than normal refractive index materials. Our results agree with those found by Islam et al.[63] and we see that MoS$_2$ has a larger refractive index than TiO$_2$ (2.48−2.62).[64]

3.3. Gibbs Free Energy. Photocatalytic water splitting can be split into two half-reactions: hydrogen evolution reaction (HER) and oxygen evolution reaction (OER), with the overall HER being able to follow two different reaction mechanisms: Volmer−Tafel and Volmer−Heyrovsky. In the Volmer step, protons are reduced to produce adsorbed hydrogen on the electrode surface. After this step, the reaction can either follow the Tafel route or the Heyrovsky route. The Volmer−Tafel reaction involves two adsorbed hydrogen atoms on the electrode surface adjacent to each other combining into a hydrogen molecule. The Volmer−Heyrovsky reaction on the other hand utilizes a proton from the surrounding water to react with an adsorbed hydrogen atom to produce a hydrogen molecule.[65]
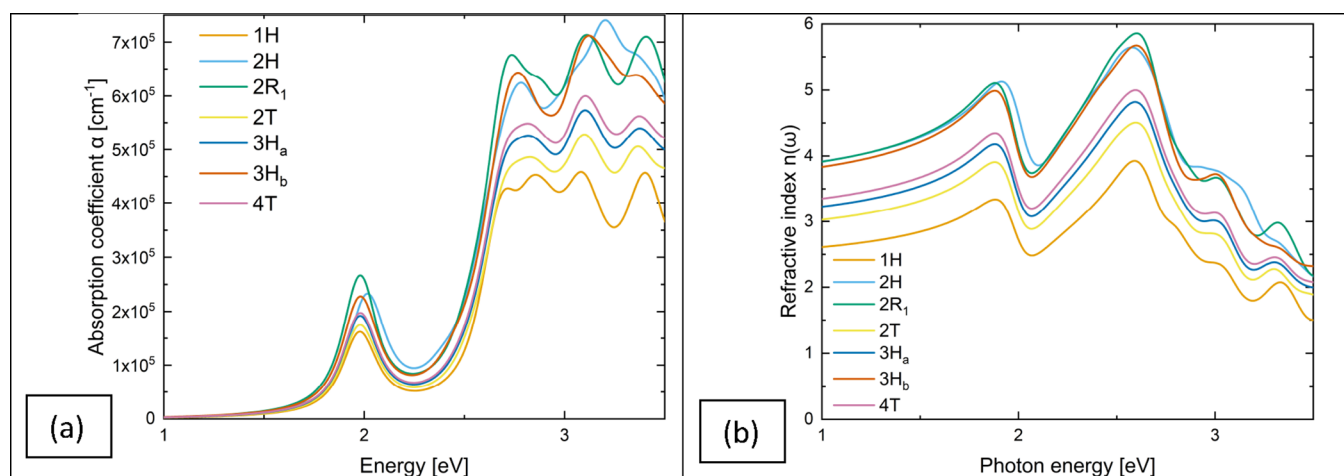
$$2H^+ + 2e^- \rightarrow 2H_{ads} \text{ (Volmer)}$$

Table 2. d-Band Center for the Stable Polymorphs

polymorph	d-band center [eV]	Fermi level [eV]
1H	0.334	−2.552
2H	0.276	3.511
2R$_1$	−1.520	3.285
2T	0.328	−0.882
3H$_a$	−1.541	0.003
3H$_b$	0.369	2.865
4T	−0.544	0.555

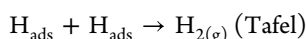**Figure 2.** Calculated absorption coefficient (a) and refractive index (b).
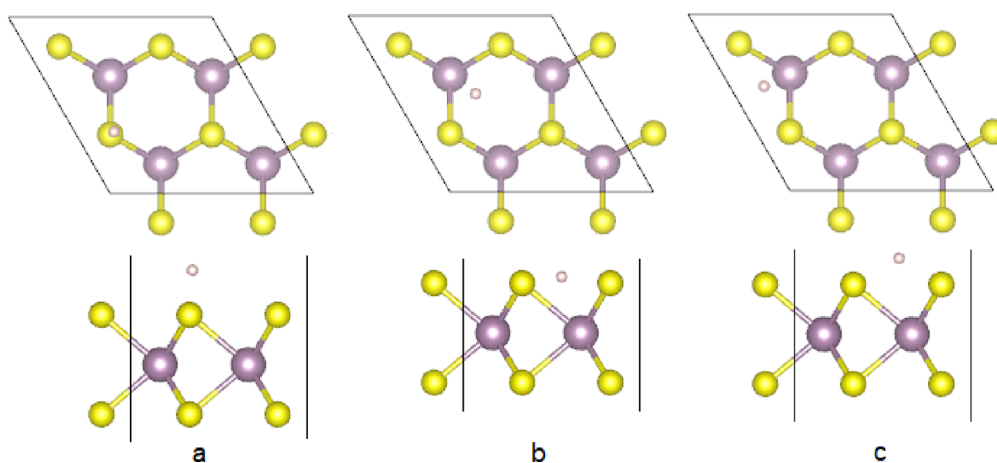
Figure 3. Location of the adsorbed hydrogen atom. (a) Top, (b) interface, and (c) bridge.

$$H_{ads} + H_{ads} \rightarrow H_{2(g)} \; (\text{Tafel})$$

$$H^+ + H_{ads} + e^- \rightarrow H_{2(g)} \; (\text{Heyrovsky})$$
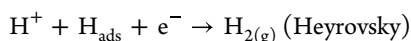
where H^+ is a proton and H_{ads} is adsorbed hydrogen atoms.

What is clear from this is that regardless of the path taken by the HER, the adsorption energy of the hydrogen atom is crucial when looking at the catalytic activity of a material. The adsorption energy of hydrogen is linked to the Gibbs free energy (ΔG_H) of hydrogen on the compound surface and is widely accepted as an indicator of catalytic activity.[66,67]

The Gibbs free energy can be calculated by the following equation:

$$\Delta G_H = E_{ads} + \Delta E_{ZPE} - T\Delta S_H$$

Here, E_{ads} is the adsorption energy, ΔE_{ZPE} is the zero-point energy difference of H_2 in the adsorbed and gas phase state with its values ranging from 0.01 to 0.04 eV, and $T\Delta S_H$ is entropy changes for finite variations at constant temperature T. For the materials we study here, ΔE_{ZPE} is set to 0.04 eV based on calculations done by Nørskov et al.[68] The value for the term ($T\Delta S_H$) can be approximated to -0.2 eV at 298 K,[69] which lets us rewrite the equation to $\Delta G_H = E_{ads} + 0.24$ eV.[68,70,71] In general, there are three possibilities for hydrogen adsorption:

1) Exothermic hydrogen adsorption: when this happens, the coverage of hydrogen atoms will be too high and the reaction will slow down.[69] This occurs for $\Delta G_H < 0$. However, the transformation can occur naturally.[72] A large and negative ΔG_H also means that H_{ads} has a weak interaction with the electrode surface and this will slow down the Volmer step, which consequently slows down the overall reaction.[67]

2) Endothermic hydrogen adsorption: here the energy barrier for proton (H^+) formation is too high.[69] $\Delta G_H > 0$. In addition, the natural direction of the reaction is opposite to what is desired (a nonspontaneous reaction).[72] Here, the H_{ads} atoms are bound strongly with the electrode surface, which makes the initial Volmer step easy. However, the following Tafel or Heyrovsky steps difficult.[67]

3) The system is at equilibrium and we have enough of all the reactants.[69,72] $\Delta G_H = 0$.

It is well known that an optimal photocatalytic material should have $\Delta G_H = 0$ and thus the adsorption energy E_{ads} should be of the order of -0.24 eV.[67,69]

We have calculated the adsorption energies of H at three different locations as it is position-dependent.[73] Our chosen locations are S top (Figure 3a), S interface (Figure 3b), and S bridge (Figure 3c). The adsorption energy was calculated as

$$E_H^{ads} = E_T[\text{system} + H] - E_T[\text{system}] - \frac{1}{2}E_{H_2}$$

where $E_T[\text{system} + \text{H}]$ represents the total energy of MoS$_2$ with an adsorbed H atom, $E_T[\text{system}]$ is the energy of MoS$_2$ without an adsorbed molecule, and E_{H_2} is the energy of a hydrogen molecule in the gas phase. The Gibbs free energies are presented in Table 3. From the calculated values, we see that there are not

Table 3. Calculated Gibbs Energy Values for the Seven Stable Polymorphs Calculated at the Three Different Locations

polymorph	bridge Gibbs [eV]	inter Gibbs [eV]	top Gibbs [eV]
1H	1.77	1.77	1.77
2H	1.75	1.75	1.85
2R$_1$	1.75	1.75	1.75
2T	1.77	1.77	1.77
3H$_a$	1.77	1.77	1.76
3H$_b$	1.75	1.75	1.75
4T	1.76	1.76	1.75

so many differences in potential catalytic activity among different polymorphs, with Gibbs values ranging from 1.75 eV to 1.85 eV. The positive values of ΔG_H indicate that the adsorbed hydrogens are bound strongly to the MoS$_2$ surface. This makes the initial Volmer step easy to undergo, while the following Tafel or Heyrovsky steps are more difficult,[67] which reduces the overall STH efficiency.

It is generally believed that the basal plane of MoS$_2$ is close to inert and it is the edges that contribute to the catalytic activity.[74] If we compare our results for the basal plane with that of Seo et al.[75] who got Gibbs energy values ranging from −0.36 to 0.66 eV for 1L, 2L, and 3L monolayer MoS$_2$ structure using the edge as active sites, this assumption appears to be true.

3.4. Doped 3H$_b$-MoS$_2$ Polymorph. 3H$_b$-MoS$_2$ was chosen over the other structures for its better electron mobility, suitable band gap, and absorption coefficient. We performed substitutional doping of both Mo atoms and S atoms. For S substitution, a doping percentage of 6.250% was chosen, while for Mo 12.5%, that is, we replaced one S atom and one Mo atom.

3.4.1. Gibbs Free Energy for Doped Polymorph. Gibbs free energies calculated for Al, Co, I, N, or Ni doped 3H$_b$-MoS$_2$ are shown in Tables 4 and 5. We found that replacing one S atom

Table 4. Gibbs Energy Values for Substitutional Doped 3H$_b$[a]

Mo replaced on 3H$_b$	bridge Gibbs [eV]	inter Gibbs [eV]	top Gibbs [eV]
Al	0.77	−0.17	0.77
Co	1.17	−0.02	1.18
I	0.73	0.29	0.73
N	−0.28	0.27	−0.28
Ni	0.96	−0.20	0.90

[a]One Mo is replaced with either one Al, Co, I, N, or Ni atom.

Table 5. Gibbs Energy Values for Substitutional Doped 3H$_b$[a]

S replaced on 3H$_b$	bridge Gibbs [eV]	inter Gibbs [eV]	top Gibbs [eV]
Al	−6.99	−6.45	−5.55
Co	−6.38	−4.83	−5.06
I	−11.18	−11.16	−11.16
N	−12.44	−12.44	−12.44
Ni	−7.46	−6.13	−6.42

[a]One S atom is replaced with either one Al, Co, I, N, or Ni atom.

with either Al, Co, I, N, or Ni decreased the Gibbs free energy; however, the values are much further away from the optimal

value (zero). In general, negative values indicate that the adsorption process is exothermic and that the surface will be flooded with hydrogen atoms, hindering the other reactants needed for a complete reaction. The large negative values also mean that the H$_{ads}$ atom has a weak interaction with the material surface, which results in a slower Volmer step and a reduced overall turnover rate.[67] Due to the size of the supercell, a smaller doping percentage was not possible, and a larger percentage was not attempted. Nonetheless, the addition of a dopant influenced the 3H$_b$-MoS$_2$ structure Gibbs free energy and electronic structure, showcasing the influence of dopants as a powerful tool in developing new photocatalysts.

When the Mo atom is substituted with a dopant atom, we see a clear improvement in the Gibbs free energy as all dopants bring it closer to zero. There is also a greater disparity between the different adsorption sites, where the best results are seen for hydrogen adsorbed at the interface (Figure 3b). This is especially significant for Co that sports a rather high Gibbs free energy for the bridge and top location (>1 eV), while for the interface site, the Gibbs free energy is −0.02 eV, making it an incredible photocatalyst when the hydrogens are adsorbed at this location. Unfortunately, it is not possible to force hydrogen to be adsorbed at specific locations. However, the hydrogen production rate must be tested experimentally before a final verdict can be cast on this compound. N-doped MoS$_2$ has on average the lowest values and they are comparable with that of the edge sites,[75] which proves that doping the basal layer of MoS$_2$ can be a valid photocatalyst.

Through doping, the electronic structure of the investigated polymorphs is changed, leading to changes in the band structures and bandgaps. Thus, GGA band structure calculations were performed to investigate how the different dopants influence the band gap. It is also important to investigate the structures' stability, band structure, and optical spectra before one can conclude whether a doped structure can perform as a photocatalyst.

3.4.2. GGA Band gaps. The electronic structure is one of the key properties when determining if a material is suitable for photocatalytic processes or photovoltaic cells as it determines the amount of absorbed sunlight.

Our GGA band gap calculations for Mo substituted with Al or I and S substituted with Co or Ni are presented in Figure 4, while the rest are seen in the Supporting Information (Figures S1 and S2). Our calculations show that only four out of the 10 doped structures are semiconductors and those are Mo substituted with Al or I and S substituted with Co or Ni. Of these four, Mo substituted with Al appears to have an intermediate bandgap.

Mo substituted with Co, N, and Ni and S substituted with Al are metals, while S substituted with N is a semi/anisotropic metal. This means that the material becomes a metal or semiconductor depending on the direction taken through the Brillouin zone, which makes them non-appropriate for photo-catalytic applications. When S is substituted with I, the material becomes an insulator making it unsuitable as a catalyst.

3.4.3. Formation Energy. We calculated the formation energy to compare the stability of the doped structures with each other. This was done with the following expression:[76]

$$\Delta H = E_{\text{doped}} - [E_{\text{structure}} + E_{\text{dopant}} - E_{\text{atom}}]$$

where E_{doped} and $E_{\text{structure}}$ are the total energies of the supercell with and without dopants, respectively, E_{dopant} is the total energy of the dopant, and E_{atom} is the total energy of the replaced atom. The results are shown below in Table 6. From these calculations,
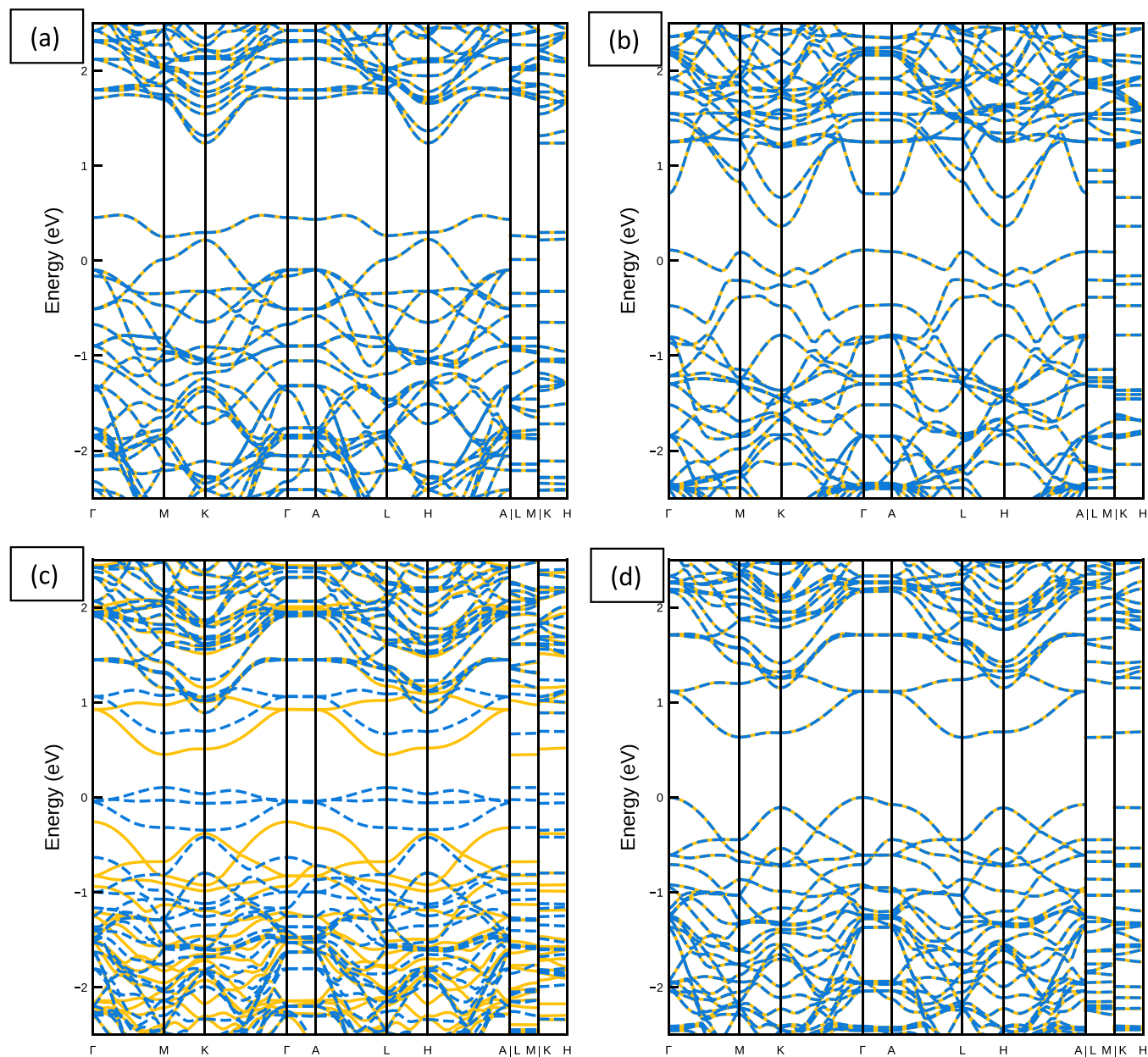
Figure 4. GGA band structures for doped $3H_b$. Here, Mo is substituted with Al (a), Mo is substituted with I (b), S is substituted with Co (c), and S is substituted with Ni (d).

Table 6. Calculated Formation Energy for the Doped $3H_b$-MoS$_2$ Structure

structure	formation energy (ΔH)
$Mo_7S_{16}Al$	3.19
$Mo_7S_{16}Co$	3.51
$Mo_7S_{16}I$	7.68
$Mo_7S_{16}N$	3.85
$Mo_7S_{16}Ni$	4.27
$Mo_8S_{15}Al$	11.13
$Mo_8S_{15}Co$	11.37
$Mo_8S_{15}I$	15.62
$Mo_8S_{15}N$	11.79
$Mo_8S_{15}Ni$	12.22

it is clear that replacing Mo with Al, Co, I, N, or Ni results in a more thermodynamically stable structure compared to replacing one S atom in $3H_b$-MoS$_2$. Mo substituted with Al appears to be the most stable of the doped structures, closely followed by Mo substituted with Co and then N. The calculated formation energies for all doped materials results are positive, which means that these compounds will not be created spontaneously and external factors (e.g., pressure, temperature, or energy) are needed to create them as the reactants are more stable than the product.

3.4.4. Mechanical Stability. In addition to influencing the electronic structure, the dopants will also affect the mechanical and dynamical stability of the polymorph. The elastic constants of a material can be used as a descriptor for how the material will react to an applied force, as either applied strain or stress. Thus, it is possible to use them to understand the mechanical stability of a material.

The stress and strain have three shear and three tensile components. Therefore, it is possible to describe the elastic

Table 7. Calculated Single-Crystal Elastic Constants C_{ij} (in GPa), Bulk Modulus B (in GPa), Shear Modulus G (in GPa), Poisson's Ratio ν, and Young's Modulus E (in GPa)[a]

polymorph	3H$_B$[25]	Al for Mo	Co for Mo	I for Mo	N for Mo	Ni for Mo	Al for S	Co for S	I for S	N for S	Ni for S
crystal system	hexagonal	hexagonal	hexagonal	hexagonal	oblique	hexagonal	hexagonal	hexagonal	hexagonal	hexagonal	hexagonal
C_{11}	176	223	161	212	254	196	301	300	296	326	302
C_{12}	45	68	72	56	−10	90	99	103	93	107	100
C_{13}	0.6	0	0	0		0	0	0	0	0	0
C_{16}					23						
C_{26}					−53						
C_{66}	46	77	44	78	116	53	101	98	101	109	101
Born	yes	yes	yes	yes	yes	yes	yes	yes	yes	yes	yes
B$_V$	50	146	116	134	119	143	200	202	195	216	201
B$_R$	2	146	116	134	117	143	200	202	195	216	201
B$_H$	26	146	116	134	118	143	200	202	195	216	201
G$_V$	34	77	44	78	123	53	101	98	101	109	101
G$_R$	0.8	77	44	78	109	53	101	98	101	109	101
G$_H$	17	77	44	78	116	53	101	98	101	109	101
E	43	202	128	197	171−292 (232)	154	268	264	267	291	269
G	17	77	44	78	103−116 (110)	53	101	98	101	109	101
ν	0.23	0.306	0.450	0.263	−0.167−0.197 (0.015)	0.462	0.329	0.345	0.315	0.328	0.330
G$_H$/B$_H$	0.653	0.527	0.379	0.582	0.932	0.370	0.505	0.485	0.518	0.505	0.502

[a]Subscript V indicates the Voigt bound, R indicates the Reuss bound, and H indicates the Hill bound.

constants of a crystal using a 6 × 6 symmetric matrix with 27 components. 21 of those 27 are independent of the others, and in addition, we can use any existing symmetry in the crystal to reduce the number of components. The stiffness matrix, C_{ij}, which the 6x6 matrix also is known as, can be used to calculate the bulk modulus, Poisson coefficient, and Lame constants. In general, it has been found that the DFT elastic constants are within 10% of the experimental values.[77]

For hexagonal polymorphs, the stability criteria are[78]

$$B_{H1} = C_{11} > |C_{12}|$$

$$B_{H2} = C_{11} > 0$$

and for oblique polymorphs the stability criteria are[78]

$$B_{O1} = C_{11} > 0$$

$$B_{O2} = C_{11}C_{22} > C_{12}C_{12}$$

$$B_{=3} = |C_{ij}| > 0$$

The 3H$_B$ structure was found to be mechanically stable with all five dopants and for both Mo and S substitutional doping as they all fulfill the Born criteria. This means that the doped structure can keep its pore size and structure under a mechanical load. To further investigate how the doped structure would react to applied mechanical forces, we used the stiffness matrix to calculate the Voigt(V), Reuss (R), and Hill (H) moduli. With these, we calculated the bulk modulus B, shear modulus G, Young's modulus E, and Poisson's ratio ν for all doped 3H$_b$-MoS$_2$ structures. The values are shown in Table 7.

Young's modulus characterizes how a structure reacts to a force applied lengthwise, both under compression and extension. All of our doped structures have positive Young's modulus ranging from 128 GPa (higher than for bronze, titanium, and annealed copper[79]) up to 291 GPa (beryllium[79]), indicating that they are quite stiff materials and would react slowly to applied pressure. To determine whether the doped

structures are ductile or brittle, we calculated the shear bulk modulus ratio, where 0.5 is the cutoff below which materials are categorized as ductile.[48] Our results show that seven of the doped structures are brittle, although three of them are just above the threshold. As they are so close to the threshold values, experimental tests would be needed to determine if MoS$_2$ structures with one S atom substituted for one Al, N, or Ni atom are brittle. Our simulations show that only when Co and Ni are substituted for Mo or Co substituted for S in 3H$_b$-MoS$_2$ do the doped materials become ductile.[80,81]

Poisson's ratio is a measure of the Poisson effect, a material's deformation perpendicular to the direction of the applied force. A value close to zero indicates that the material's structure (e.g., foam) would collapse in the compression, while materials with a much larger bulk modulus than shear modulus (rubber) will have a Poisson ratio around 0.5.[82] Co and Ni substitutions for Mo have quite high values (0.450 and 0.462), putting them in the upper region together with gold and saturated clay. I substitution for Mo on the other hand is in the mid-range where similar materials would be magnesium and variants of cast iron. The rest are in the range of 0.306 to 0.345, which is similar to the Poisson ratio of stainless steel, aluminum alloy and copper. Compared to the values obtained for 3H$_b$ in our previous paper, we see that the shear modulus has increased for the doped structures, indicating that they will withstand higher values of shear stress. Adding dopants has also made the structures ductile in the case of Co and Ni substitution for Mo and Co substitution for S. This showcases the power of doping when it comes to altering and improving mechanical properties of materials.

3.4.5. Dynamical Stability. It is not enough for a material to be mechanically stable; it must also be dynamically stable. To verify this, we performed phonon and phonon density of states calculations. In addition, we have calculated the phonon dispersion curves, at the equilibrium volume, along the high symmetry direction of the Brillouin zone and these results are seen in Figures 5 and 6. The 3H$_b$ structures where one Mo atom
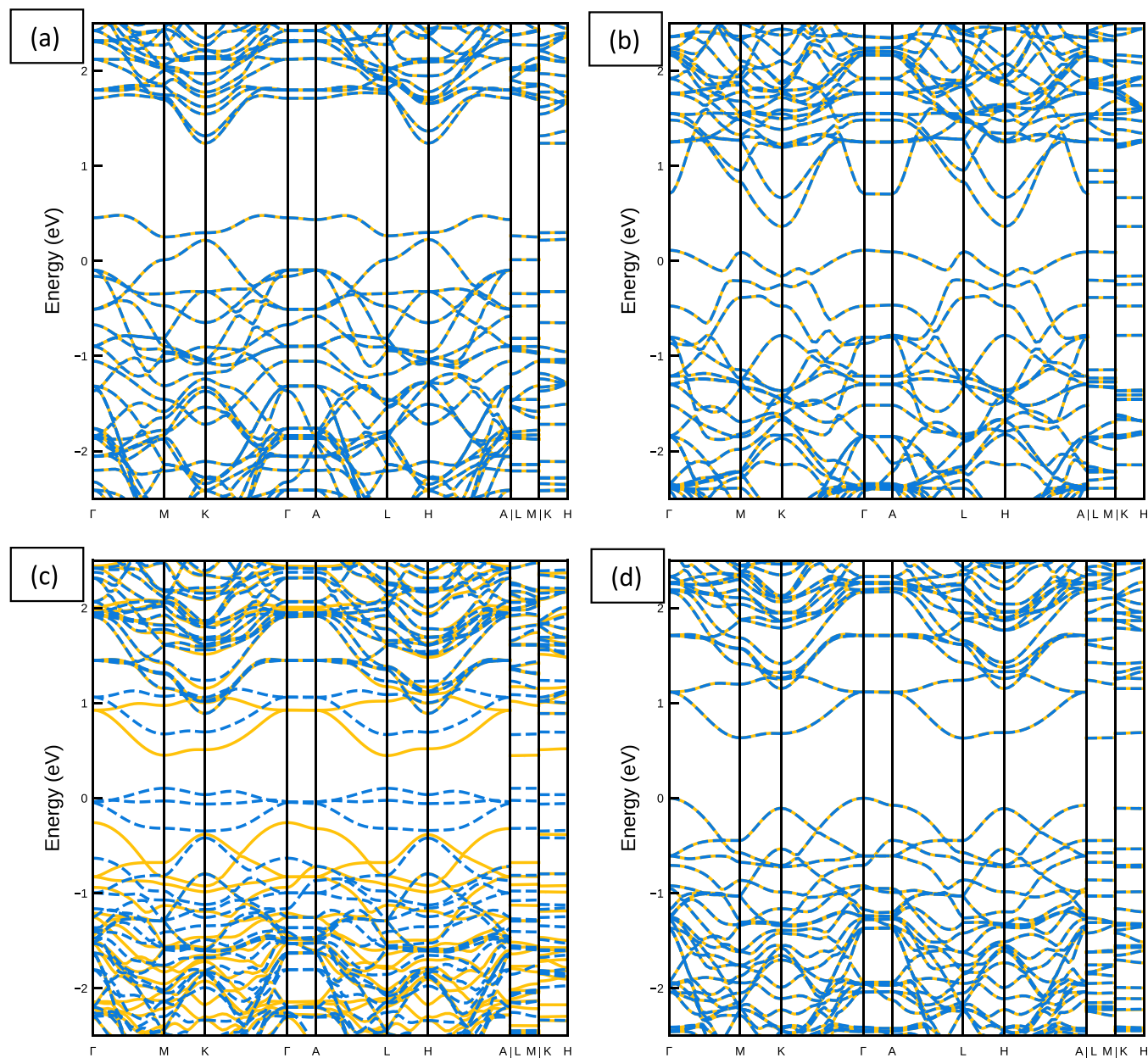
Figure 5. Phonon density of states for 3H$_b$ doped with Al (a), Co (b), I (c), N (d), and Ni (e) for Mo.

was replaced with one Co, I, or one N atom have clear and distinctive negative frequencies, as seen in Figure 5b−d, respectively, which makes the dynamically unstable structures.

In general, if a material is mechanically stable and dynamically unstable, it could have a metastable phase and by using dopants, nanoparticles and nanoobjects the structures can be stabilized.

For Mo replaced with either one Al or one Ni atom, small and similar negative modes are seen for both structures between A-L, M-Γ, Γ-K, and H-A.

The imaginary modes seen in Figure 5a,e are believed to be caused by lattice distortions stemming from the creation of the supercell. The effect of these distortions can potentially be dealt with by changing the supercell size. Phonon calculations also require extremely (10^{-8}) accurate forces,[83] while the volume relaxation calculations were performed using 10^{-6} as the accuracy limit. This difference in accuracy could have caused these small imaginary modes we see for Al or Ni. Another possible explanation is a slightly wrong magnetic moment in the

input files for the phonon calculations. Wolloch et al. found that quite small differences in the magnetic moment can help stabilize a structure.[83] Based on this, we conclude that these two structures are dynamically stable.

For the S-substituted structures presented in Figure 6, we see the same type of negative modes, as seen in Figure 5a,e, appear for S replaced with Mo (Figure 6a) and I (Figure 6c). While for S replaced with either Co, N, or Ni, Figure 6b,d,e respectively, the negative frequency is near zero and an artifact from the calculations. Thus, we can conclude that all the S-substituted structures are dynamically stable.
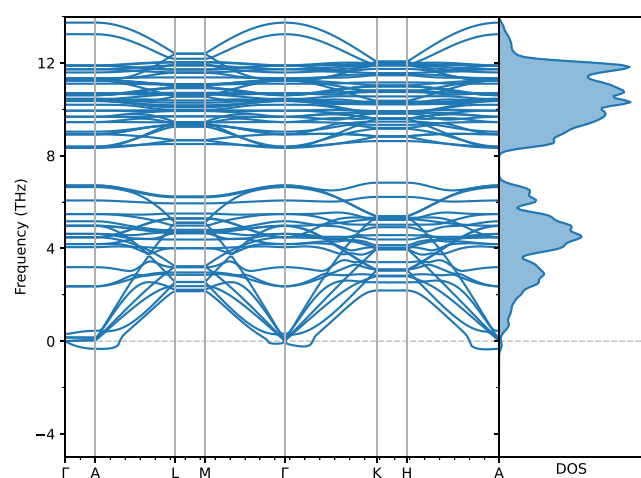
3.4.6. Charge Density Calculations. The charge density map shown in Figure 7a for 3H$_b$-MoS$_2$ clearly shows that the electrons reside around the individual atoms. In addition, the spherically shaped charge distribution indicates that the bonding between Mo−S and S−S is primarily ionic. The charge transfer plots in Figure 7b reveal a depletion of charge around the Mo atoms, while we get a charge accumulation around the S atoms
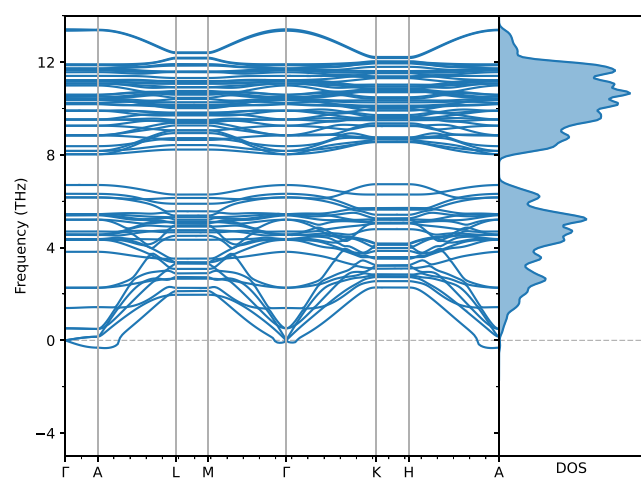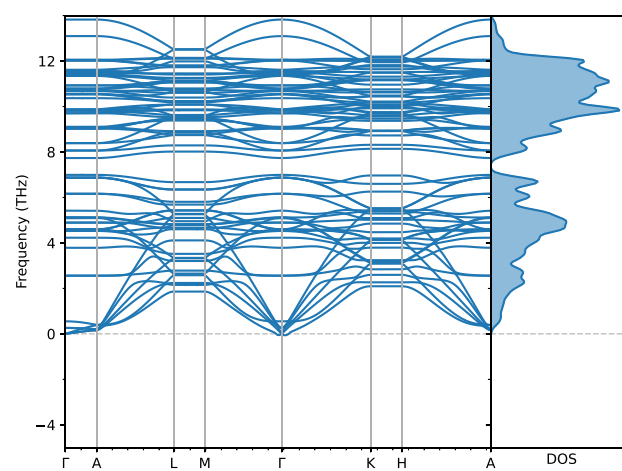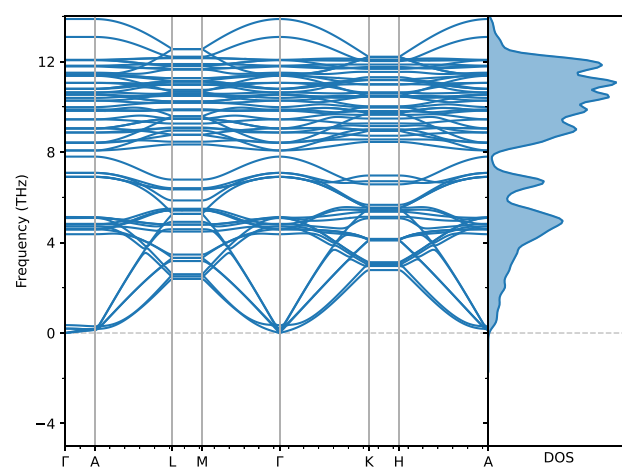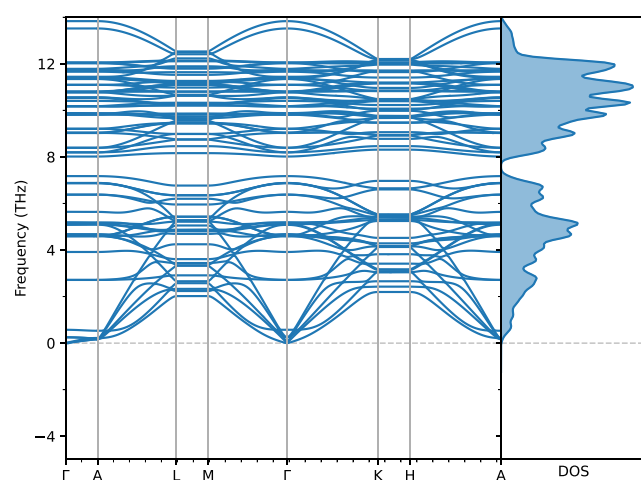
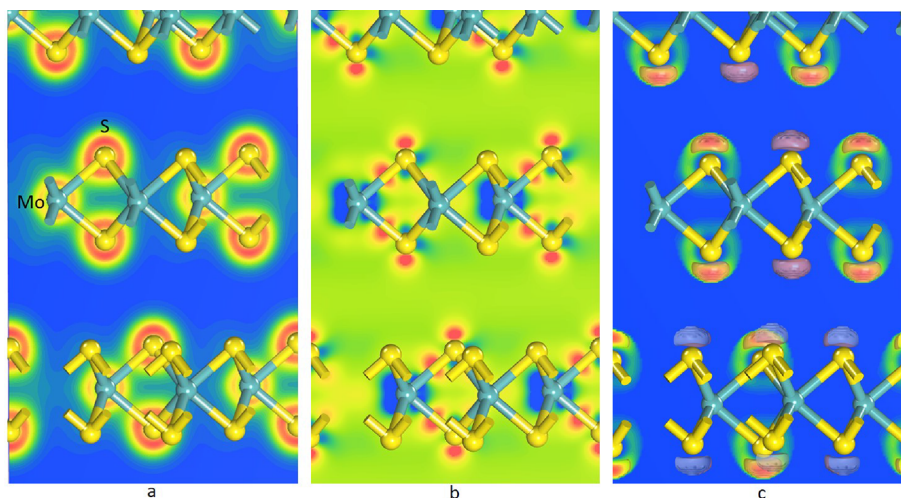**Figure 6.** Phonon density of states for $3H_b$ with S substituted for Al (a), Co (b), I (c), N (d), and Ni (e).

Figure 7. Calculated charge density map (a), charge transfer plot (b), and electron localization function (c) for $3H_b$-MoS$_2$.

and between the Mo and S atoms. As the charge transfer plot shows, the charge gathers around the S atoms and indicates a slight polar character for the compound The electron localization function (ELF), Figure 7c, is a measure of the spatial localization of electrons that helps to map electron pair probability in multielectron systems. Our ELF findings are consistent with that of the charge transfer plot, and we can thus expect the electron to be found outside of the S atoms.

4. CONCLUSIONS

Seven MoS$_2$ polymorphs were studied with regard to phase transition and their photocatalytic capabilities were analyzed using catalytic indicators such as d-band center, Gibbs free energy, and absorption coefficient. The most promising candidate, $3H_b$-MoS$_2$, was chosen for further enquiries and was substitutionally doped with Al, Co, I, N, and Ni atoms at two different locations. This study shows the following:

- No phase transitions caused by temperature changes were found for 1H, 2H, 2R$_1$, 2T, 3H$_a$, 3H$_b$, and 4T polymorphs.
- All seven polymorphs have their absorption peak at 620 nm in the visible spectra.
  - 2R$_1$ has the highest maximum (2.67×10^5 cm^{-1}) followed by 2H and 3H$_b$ at 2.33×10^5 and 2.28×10^5 cm^{-1}, respectively.
- 2R$_1$, 2H, 3H$_b$, 4T, and 3H$_a$ are the high refractive index materials ($n > 3.9$).
- Different dopants of $3H_b$-MoS$_2$ resulted in varying band gaps.
  - Only four were seen to be semiconductors: Mo substituted with Al and I and S substituted with Co and Ni.
  - S substituted with I is an insulator.
  - The remaining five structures, Mo substituted with Co, N, or Ni and S substituted with Al or N, are metallic.
- Mo substitutional doped MoS$_2$ with Al, Co, I, N, and Ni reduces the Gibbs free energy by a factor of 10.
  - $3H_b$-MoS$_2$ doped with N for Mo ($-0.28-0.27$ eV) has a lower Gibbs free energy than the edge sites of MoS$_2$.
- Only Co, I, and N for Mo-doped $3H_b$-MoS$_2$ are dynamically unstable.

- The other seven structures are both mechanically and dynamically stable.
- Structures with Mo replaced are more thermodynamically stable than structures with S substituted.

Our calculations show that $3H_b$-MoS$_2$ doped with Al and Ni for one Mo atom and $3H_b$-MoS$_2$ doped with Al, Co, I, N, and Ni for one S atom are dynamically and mechanically stable. This makes it possible to synthesize and perform experimental tests on these structures. Through doping, we lowered the Gibbs free energy of $3H_b$-MoS$_2$ and made the basal plane competitive with the edge sites, especially for N for Mo. Our study indicates that $3H_b$-MoS$_2$ substitutionally doped with Al for Mo atoms is a promising candidate for photocatalytic water splitting. However, the best doping percentage and optimal dopant need to be found through further theoretical and experimental studies. Future work should also investigate if the dopants introduce new photocatalytic sites and through that increases the overall STH efficiency. In addition, it should be looked into if the dopant promotes carrier separation and carrier mobility.

■ ASSOCIATED CONTENT

Ⓢ Supporting Information

The Supporting Information is available free of charge at https://pubs.acs.org/doi/10.1021/acsomega.3c02623.

> GGA band structure for $3H_b$-MoS$_2$ substitutional doped with Al, Co, I, N, and Ni for either one Mo atom or one S atom (PDF)

■ AUTHOR INFORMATION

Corresponding Author

Håkon Eidsvåg − *Department of Computing, Mathematics and Physics, Western Norway University of Applied Sciences, 5063 Bergen, Norway;* Present Address: Present address: NORCE Norwegian Research Centre AS, Nygårdsgaten 112, 5008 Bergen, Norway; ⓞ orcid.org/0000-0001-6831-0695; Email: heid@hvl.no

Authors

Ponniah Vajeeston − *Department of Chemistry, Center for Materials Science and Nanotechnology, University of Oslo, N-0315 Oslo, Norway*

Dhayalan Velauthapillai − *Department of Computing, Mathematics and Physics, Western Norway University of*

Applied Sciences, 5063 Bergen, Norway; ● orcid.org/0000-0002-4162-7446

Complete contact information is available at:
https://pubs.acs.org/10.1021/acsomega.3c02623

Author Contributions

H.E.: conceptualization, methodology, software, formal analysis, writing − original draft, writing − review & editing, and visualization; D.V.: supervision, resources, validation, writing − review and editing; P.V.: validation, supervision, writing − review and editing.

Notes

The authors declare no competing financial interest.

■ ACKNOWLEDGMENTS

■ REFERENCES

(1) Chen, W.-H.; Lee, J. E.; Jang, S.-H.; Lam, S.-S.; Rhee, G. H.; Jeon, K.-J.; Hussain, M.; Park, Y.-K. A Review on the Visible Light Active Modified Photocatalysts for Water Splitting for Hydrogen Production. *Int. J. Energy Res.* **2022**, *46*, 5467−5477.

(2) Jafari, T.; Moharreri, E.; Amin, A. S.; Miao, R.; Song, W.; Suib, S. L. Photocatalytic Water Splitting-The Untamed Dream: A Review of Recent Advances. *Molecules* **2016**, *21*, 900.

(3) Steinfeld, A. Solar Hydrogen Production via a Two-Step Water-Splitting Thermochemical Cycle Based on Zn/ZnO Redox Reactions. *Int. J. Hydrogen Energy* **2002**, *27*, 611−619.

(4) Kudo, A. Photocatalysis and Solar Hydrogen Production. *Pure Appl. Chem.* **2007**, *79*, 1917−1927.

(5) Fajrina, N.; Tahir, M. A Critical Review in Strategies to Improve Photocatalytic Water Splitting towards Hydrogen Production. *Int. J. Hydrogen Energy* **2019**, *44*, 540−577.

(6) Wang, Q.; Domen, K. Particulate Photocatalysts for Light-Driven Water Splitting: Mechanisms, Challenges, and Design Strategies. *Chem. Rev.* **2020**, *120*, 919−985.

(7) Gupta, U.; Rao, C. N. R. Hydrogen Generation by Water Splitting Using MoS2 and Other Transition Metal Dichalcogenides. *Nano Energy* **2017**, *41*, 49−65.

(8) Li, S.; Wang, S.; Salamone, M. M.; Robertson, A. W.; Nayak, S.; Kim, H.; Tsang, S. C. E.; Pasta, M.; Warner, J. H. Edge-Enriched 2D MoS2 Thin Films Grown by Chemical Vapor Deposition for Enhanced Catalytic Performance. *ACS Catal.* **2017**, *7*, 877−886.

(9) Ji, X.; Lin, Y.; Zeng, J.; Ren, Z.; Lin, Z.; Mu, Y.; Qiu, Y.; Yu, J. Graphene/MoS2/FeCoNi(OH)x and Graphene/MoS2/FeCoNiPx Multilayer-Stacked Vertical Nanosheets on Carbon Fibers for Highly Efficient Overall Water Splitting. *Nat. Commun.* **2021**, *12*, 1380.

(10) Chen, T.-Y.; Chang, Y.-H.; Hsu, C.-L.; Wei, K.-H.; Chiang, C.-Y.; Li, L.-J. Comparative Study on MoS2 and WS2 for Electrocatalytic Water Splitting. *Int. J. Hydrogen Energy* **2013**, *38*, 12302−12309.

(11) Jaleel UC, J. R.; R, M.; Devi K R, S.; Pinheiro, D.; Mohan, M. K. Structural, Morphological and Optical Properties of MoS2-Based Materials for Photocatalytic Degradation of Organic Dye. *Photochem* **2022**, *2*, 628−650.

(12) Gawari, D.; Pandit, V.; Jawale, N.; Kamble, P. Layered MoS2 for Photocatalytic Dye Degradation. *Mater. Today: Proc.* **2022**, *53*, 10−14.

(13) Chen, L.; Hsieh, S.-L.; Kuo, C.-H.; Hsieh, S.; Chen, W.-H.; Chen, C.-W.; Dong, C.-D. Novel MoS2 Quantum Dots as a Highly Efficient Visible-Light Driven Photocatalyst in Water Remediation. *RSC Adv.* **2020**, *10*, 31794−31799.

(14) Sivaranjani, P. R.; Janani, B.; Thomas, A. M.; Raju, L. L.; Khan, S. S. Recent Development in MoS2-Based Nano-Photocatalyst for the Degradation of Pharmaceutically Active Compounds. *J. Cleaner Prod.* **2022**, *352*, No. 131506.

(15) Voiry, D.; Salehi, M.; Silva, R.; Fujita, T.; Chen, M.; Asefa, T.; Shenoy, V. B.; Eda, G.; Chhowalla, M. Conducting MoS2 Nanosheets as Catalysts for Hydrogen Evolution Reaction. *Nano Lett.* **2013**, *13*, 6222−6227.

(16) Lukowski, M. A.; Daniel, A. S.; Meng, F.; Forticaux, A.; Li, L.; Jin, S. Enhanced Hydrogen Evolution Catalysis from Chemically Exfoliated Metallic MoS2 Nanosheets. *J. Am. Chem. Soc.* **2013**, *135*, 10274−10277.

(17) Wang, H.; Lu, Z.; Xu, S.; Kong, D.; Cha, J. J.; Zheng, G.; Hsu, P.-C.; Yan, K.; Bradshaw, D.; Prinz, F. B.; Cui, Y. Electrochemical Tuning of Vertically Aligned MoS2 Nanofilms and Its Application in Improving Hydrogen Evolution Reaction. *Proc. Natl. Acad. Sci.* **2013**, *110*, 19701−19706.

(18) Lv, Y.; Chen, P.; Foo, J. J.; Zhang, J.; Qian, W.; Chen, C.; Ong, W.-J. Dimensionality-Dependent MoS2 toward Efficient Photocatalytic Hydrogen Evolution: From Synthesis to Modifications in Doping, Surface and Heterojunction Engineering. *Mater. Today Nano* **2022**, *18*, No. 100191.

(19) Shi, X.; Zhang, M.; Wang, X.; Kistanov, A. A.; Li, T.; Cao, W.; Huttula, M. Nickel Nanoparticle-Activated MoS2 for Efficient Visible Light Photocatalytic Hydrogen Evolution. *Nanoscale* **2022**, *14*, 8601−8610.

(20) Liu, M.; Zhang, C.; Han, A.; Wang, L.; Sun, Y.; Zhu, C.; Li, R.; Ye, S. Modulation of Morphology and Electronic Structure on MoS2-Based Electrocatalysts for Water Splitting. *Nano Res.* **2022**, *15*, 6862−6887.

(21) Zhao, H.; Jian, L.; Gong, M.; Jing, M.; Li, H.; Mao, Q.; Lu, T.; Guo, Y.; Ji, R.; Chi, W.; Dong, Y.; Zhu, Y. Transition-Metal-Based Cocatalysts for Photocatalytic Water Splitting. *Small Struct.* **2022**, *3*, No. 2100229.

(22) Khan, M. M.; Rahman, A. Chalcogenides and Chalcogenide-Based Heterostructures as Photocatalysts for Water Splitting. *Catalysts* **2022**, *12*, 1338.

(23) Zang, Y.; Niu, S.; Wu, Y.; Zheng, X.; Cai, J.; Ye, J.; Xie, Y.; Liu, Y.; Zhou, J.; Zhu, J.; Liu, X.; Wang, G.; Qian, Y. Tuning Orbital Orientation Endows Molybdenum Disulfide with Exceptional Alkaline Hydrogen Evolution Capability. *Nat. Commun.* **2019**, *10*, 1217.

(24) Zhong, W.; Gao, D.; Wang, P.; Wang, X.; Yu, H. Accelerating Hydroxyl Desorption by Swapping Catalytic Sites in RuMoS2+x Cocatalysts for Efficient Alkaline Photocatalytic H2 Production. *Appl. Catal., B* **2022**, *319*, No. 121910.

(25) Eidsvåg, H.; Rasukkannu, M.; Velauthapillai, D.; Vajeeston, P. In-Depth First-Principle Study on Novel MoS2 Polymorphs. *RSC Adv.* **2021**, *11*, 3759−3769.

(26) Vandalon, V.; Verheijen, M. A.; Kessels, W. M. M.; Bol, A. A. Atomic Layer Deposition of Al-Doped MoS2: Synthesizing a p-Type 2D Semiconductor with Tunable Carrier Density. *ACS Appl. Nano Mater.* **2020**, *3*, 10200−10208.

(27) Li, D.; Li, W.; Zhang, J. Al Doped MoS2 Monolayer: A Promising Low-Cost Single Atom Catalyst for CO Oxidation. *Appl. Surf. Sci.* **2019**, *484*, 1297−1303.

(28) Liang, Z.; Xue, Y.; Wang, X.; Zhou, Y.; Zhang, X.; Cui, H.; Cheng, G.; Tian, J. Co Doped MoS2 as Cocatalyst Considerably Improved Photocatalytic Hydrogen Evolution of G-C3N4 in an Alkalescent Environment. *Chem. Eng. J.* **2021**, *421*, No. 130016.

(29) Dai, X.; Du, K.; Li, Z.; Liu, M.; Ma, Y.; Sun, H.; Zhang, X.; Yang, Y. Co-Doped MoS2 Nanosheets with the Dominant CoMoS Phase Coated on Carbon as an Excellent Electrocatalyst for Hydrogen Evolution. *ACS Appl. Mater. Interfaces* **2015**, *7*, 27242−27253.

(30) Yang, Y.-Q.; Zhao, C.-X.; Bai, S.-Y.; Wang, C.-P.; Niu, C.-Y. Activating MoS2 Basal Planes for Hydrogen Evolution through the As Doping and Strain. *Phys. Lett. A* **2019**, *383*, 2997−3000.

(31) Yang, Q.; Wang, Z.; Dong, L.; Zhao, W.; Jin, Y.; Fang, L.; Hu, B.; Dong, M. Activating MoS2 with Super-High Nitrogen-Doping Concentration as Efficient Catalyst for Hydrogen Evolution Reaction. *J. Phys. Chem. C* **2019**, *123*, 10917−10925.

(32) Wang, D.; Zhang, X.; Shen, Y.; Wu, Z. Ni-Doped MoS2 Nanoparticles as Highly Active Hydrogen Evolution Electrocatalysts. *RSC Adv.* **2016**, *6*, 16656−16661.

(33) Zhang, R.; Zhang, M.; Yang, H.; Li, G.; Xing, S.; Li, M.; Xu, Y.; Zhang, Q.; Hu, S.; Liao, H.; Cao, Y. Creating Fluorine-Doped MoS2 Edge Electrodes with Enhanced Hydrogen Evolution Activity. *Small Methods* **2021**, *5*, No. 2100612.

(34) Hohenberg, P.; Kohn, W. Inhomogeneous Electron Gas. *Phys. Rev.* **1964**, *136*, B864−B871.

(35) Kohn, W.; Sham, L. J. Self-Consistent Equations Including Exchange and Correlation Effects. *Phys. Rev.* **1965**, *140*, A1133−A1138.

(36) Kresse, G.; Furthmüller, J. Efficient Iterative Schemes for Ab Initio Total-Energy Calculations Using a Plane-Wave Basis Set. *Phys. Rev. B* **1996**, *54*, 11169−11186.

(37) Kresse, G.; Joubert, D. From Ultrasoft Pseudopotentials to the Projector Augmented-Wave Method. *Phys. Rev. B* **1999**, *59*, 1758−1775.

(38) Perdew, J. P.; Burke, K.; Ernzerhof, M. Generalized Gradient Approximation Made Simple. *Phys. Rev. Lett.* **1996**, *77*, 3865−3868.

(39) Blöchl, P. E. Projector Augmented-Wave Method. *Phys. Rev. B* **1994**, *50*, 17953−17979.

(40) Andrinopoulos, L.; Hine, N. D. M.; Mostofi, A. A. Calculating Dispersion Interactions Using Maximally Localized Wannier Functions. *J. Chem. Phys.* **2011**, *135*, 154105.

(41) Silvestrelli, P. L. Van Der Waals Interactions in DFT Made Easy by Wannier Functions. *Phys. Rev. Lett.* **2008**, *100*, No. 053002.

(42) Silvestrelli, P. L. Van Der Waals Interactions in Density Functional Theory Using Wannier Functions. *J. Phys. Chem. A* **2009**, *113*, 5224−5234.

(43) Togo, A.; Tanaka, I. First Principles Phonon Calculations in Materials Science. *Scr. Mater.* **2015**, *108*, 1−5.

(44) Ravindran, P.; Vidya, R.; Kjekshus, A.; Fjellvåg, H.; Eriksson, O. Theoretical Investigation of Magnetoelectric Behavior in BiFeO3. *Phys. Rev. B* **2006**, *74*, No. 224412.

(45) Heyd, J.; Scuseria, G. E.; Ernzerhof, M. Hybrid Functionals Based on a Screened Coulomb Potential. *J. Chem. Phys.* **2003**, *118*, 8207−8215.

(46) Wang, V.; Xu, N.; Liu, J.-C.; Tang, G.; Geng, W.-T. VASPKIT: A User-Friendly Interface Facilitating High-Throughput Computing and Analysis Using VASP Code. *Comput. Phys. Commun.* **2021**, *267*, No. 108033.

(47) Ganose, A. M.; Jackson, A. J.; Scanlon, D. O. Sumo: Command-Line Tools for Plotting and Analysis of Periodic *ab Initio* Calculations. *J. Open Source Software* **2018**, *3*, 717.

(48) Kirchner-Hall, N. E.; Zhao, W.; Xiong, Y.; Timrov, I.; Dabo, I. Extensive Benchmarking of DFT+U Calculations for Predicting Band Gaps. *Appl. Sci.* **2021**, *11*, 2395.

(49) O'Rourke, C.; Bowler, D. R. Intrinsic Oxygen Vacancy and Extrinsic Aluminum Dopant Interplay: A Route to the Restoration of Defective TiO2. *J. Phys. Chem. C* **2014**, *118*, 7261−7271.

(50) Farkaš, B.; Santos-Carballal, D.; Cadi-Essadek, A.; de Leeuw, N. H. A DFT+U Study of the Oxidation of Cobalt Nanoparticles: Implications for Biomedical Applications. *Materialia* **2019**, *7*, No. 100381.

(51) Welch, E.; Scolfaro, L.; Zakhidov, A. Density Functional Theory + U Modeling of Polarons in Organohalide Lead Perovskites. *AIP Adv.* **2016**, *6*, 125037.

(52) Parhizgar, S. S.; Beheshtian, J. Effect of Nitrogen Doping on Electronic and Optical Properties of ZnO Sheet: DFT+U Study. *Comput. Condens. Matter* **2018**, *15*, 1−6.

(53) Yu, M.; Yang, S.; Wu, C.; Marom, N. Machine Learning the Hubbard U Parameter in DFT+U Using Bayesian Optimization. *npj Comput. Mater.* **2020**, *6*, 180.

(54) Hammer, B.; Nørskov, J. K. Why Gold Is the Noblest of All the Metals. *Nature* **1995**, *376*, 238−240.

(55) Hammer, B.; Nørskov, J. K. Electronic Factors Determining the Reactivity of Metal Surfaces. *Surf. Sci.* **1995**, *343*, 211−220.

(56) Zheng, J.; Sheng, W.; Zhuang, Z.; Xu, B.; Yan, Y. Universal Dependence of Hydrogen Oxidation and Evolution Reaction Activity of Platinum-Group Metals on PH and Hydrogen Binding Energy. *Sci. Adv.* **2016**, *2*, No. e1501602.

(57) Nørskov, J. K.; Abild-Pedersen, F.; Studt, F.; Bligaard, T. Density Functional Theory in Surface Chemistry and Catalysis. *Proc. Natl. Acad. Sci.* **2011**, *108*, 937−943.

(58) Guo, Q.; Liang, F.; Sun, Z.; Wang, Y.; Li, X.-B.; Xia, S.-G.; Zhang, Z. C.; Huang, L.; Wu, L.-Z. Optimal D-Band-Induced Cu3N as a Cocatalyst on Metal Sulfides for Boosting Photocatalytic Hydrogen Evolution. *J. Mater. Chem. A* **2020**, *8*, 22601−22606.

(59) Zhou, Y.; Qin, W.; Sun, X.; Zhu, Y.; Niu, J. Synergistic Effects on D-Band Center via Coordination Sites of M-N3P1 (M = Co and Ni) in Dual Single Atoms That Enhances Photocatalytic Dechlorination from Tetrachlorobispheonl A. *J. Hazard. Mater.* **2022**, *430*, No. 128419.

(60) Chen, C. T.; Pedrini, J.; Gaulding, E. A.; Kastl, C.; Calafiore, G.; Dhuey, S.; Kuykendall, T. R.; Cabrini, S.; Toma, F. M.; Aloni, S.; Schwartzberg, A. M. Very High Refractive Index Transition Metal Dichalcogenide Photonic Conformal Coatings by Conversion of ALD Metal Oxides. *Sci. Rep.* **2019**, *9*, 2768.

(61) Born, M.; Wolf, E. *Principles of Optics: Electromagnetic Theory of Propagation, Interference and Diffraction of Light*; 7th (expanded) ed.; 13th printing; Cambridge University Press: Cambridge, 2017.

(62) Coccioli, R.; Boroditsky, M.; Kim, K. W.; Rahmat-Samii, Y.; Yablonovitch, E. Smallest Possible Electromagnetic Mode Volume in a Dielectric Cavity. *IEE Proc.: Optoelectron.* **1998**, *145*, 391−397.

(63) Islam, K. M.; Synowicki, R.; Ismael, T.; Oguntoye, I.; Grinalds, N.; Escarra, M. D. In-Plane and Out-of-Plane Optical Properties of Monolayer, Few-Layer, and Thin-Film MoS2 from 190 to 1700 Nm and Their Application in Photonic Device Design. *Adv. Photonics Res.* **2021**, *2*, No. 2000180.

(64) Möls, K.; Aarik, L.; Mändar, H.; Kasikov, A.; Niilisk, A.; Rammula, R.; Aarik, J. Influence of Phase Composition on Optical Properties of TiO2: Dependence of Refractive Index and Band Gap on Formation of TiO2-II Phase in Thin Films. *Opt. Mater.* **2019**, *96*, No. 109335.

(65) Kakaei, K.; Esrafili, M. D.; Ehsani, A. Alcohol Oxidation and Hydrogen Evolution. In *Interface Science and Technology*; Kakaei, K.; Esrafili, M. D.; Ehsani, A., Eds.; Graphene Surfaces; Elsevier, 2019; Vol. 27, pp. 253−301. DOI: 10.1016/B978-0-12-814523-4.00007-1.

(66) Tang, Q.; Jiang, D. Mechanism of Hydrogen Evolution Reaction on 1T-MoS2 from First Principles. *ACS Catal.* **2016**, *6*, 4953−4961.

(67) Zou, X.; Zhang, Y. Noble Metal-Free Hydrogen Evolution Catalysts for Water Splitting. *Chem. Soc. Rev.* **2015**, *44*, 5148−5180.

(68) Nørskov, J. K.; Bligaard, T.; Logadottir, A.; Kitchin, J. R.; Chen, J. G.; Pandelov, S.; Stimming, U. Trends in the Exchange Current for Hydrogen Evolution. *J. Electrochem. Soc.* **2005**, *152*, J23.

(69) Greeley, J.; Nørskov, J. K.; Kibler, L. A.; El-Aziz, A. M.; Kolb, D. M. Hydrogen Evolution Over Bimetallic Systems: Understanding the Trends. *ChemPhysChem* **2006**, *7*, 1032−1035.

(70) Tan, T. L.; Wang, L.-L.; Johnson, D. D.; Bai, K. A Comprehensive Search for Stable Pt−Pd Nanoalloy Configurations and Their Use as Tunable Catalysts. *Nano Lett.* **2012**, *12*, 4875−4880.

(71) Mir, S. H.; Chakraborty, S.; Jha, P. C.; Wärnå, J.; Soni, H.; Jha, P. K.; Ahuja, R. Two-Dimensional Boron: Lightest Catalyst for Hydrogen and Oxygen Evolution Reaction. *Appl. Phys. Lett.* **2016**, *109*, No. 053903.

(72) Castellan, G. W. *Physical Chemistry*; 3rd ed.; Addison-Wesley: Reading, Mass, 1983.

(73) Pan, H.; Feng, Y. P.; Lin, J. Hydrogen Adsorption by Tungsten Carbide Nanotube. *Appl. Phys. Lett.* **2007**, *90*, 223104.

(74) Zhu, J.; Wang, Z.-C.; Dai, H.; Wang, Q.; Yang, R.; Yu, H.; Liao, M.; Zhang, J.; Chen, W.; Wei, Z.; Li, N.; Du, L.; Shi, D.; Wang, W.; Zhang, L.; Jiang, Y.; Zhang, G. Boundary Activated Hydrogen Evolution Reaction on Monolayer MoS2. *Nat. Commun.* **2019**, *10*, 1348.

(75) Seo, B.; Jung, G. Y.; Sa, Y. J.; Jeong, H. Y.; Cheon, J. Y.; Lee, J. H.; Kim, H. Y.; Kim, J. C.; Shin, H. S.; Kwak, S. K.; Joo, S. H. Monolayer-Precision Synthesis of Molybdenum Sulfide Nanoparticles and Their Nanoscale Size Effects in the Hydrogen Evolution Reaction. *ACS Nano* **2015**, *9*, 3728−3739.

(76) Martínez, N.; Martínez, J. A. R. First-Principles Study on the Formation Energies of $Ga_{1-x}Cr_xAs$. *J. Phys.: Conf. Ser.* **2016**, *743*, No. 012007.

(77) Ravindran, P.; Fast, L.; Korzhavyi, P. A.; Johansson, B.; Wills, J.; Eriksson, O. Density Functional Theory for Calculation of Elastic Properties of Orthorhombic Crystals: Application to TiSi2. *J. Appl. Phys.* **1998**, *84*, 4891−4904.

(78) Wang, V.; Tang, G.; Wang, R.-T.; Liu, Y.-C.; Liang, Y.-Y.; Kawazoe, Y.; Nara, J.; Geng, W.-T. High-Throughput Computational Screening of 2D Semiconductors and Heterostructures for Photo-catalytic Water Splitting. *arXiv e-prints* **2022**, arXiv-1806.

(79) Engineering ToolBox *Young's Modulus, Tensile Strength and Yield Strength Values for Some Materials*; Engineering ToolBox, 2003, *2020*. https://www.engineeringtoolbox.com/young-modulus-d_417.html.

(80) Goldstein, R. V.; Gorodtsov, V. A.; Lisovenko, D. S. Variability of Elastic Properties of Hexagonal Auxetics. *Dokl. Phys.* **2011**, *56*, 602−605.

(81) Pugh, S. F. XCII. Relations between the Elastic Moduli and the Plastic Properties of Polycrystalline Pure Metals. *London, Edinburgh, Dublin Philos. Mag. J. Sci.* **1954**, *45*, 823−843.

(82) Jastrzebski, Z. D. *The Nature of Properties of Engineering Materials*; 3rd ed.; John Wiley and Sons Ltd., 1987.

(83) Wolloch, M.; Gruner, M. E.; Keune, W.; Mohn, P.; Redinger, J.; Hofer, F.; Suess, D.; Podloucky, R.; Landers, J.; Salamon, S.; Scheibel, F.; Spoddig, D.; Witte, R.; Roldan Cuenya, B.; Gutfleisch, O.; Hu, M. Y.; Zhao, J.; Toellner, T.; Alp, E. E.; Siewert, M.; Entel, P.; Pentcheva, R.; Wende, H. Impact of Lattice Dynamics on the Phase Stability of Metamagnetic FeRh: Bulk and Thin Films. *Phys. Rev. B* **2016**, *94*, No. 174435.